Scientific Research Publishing

Advances in Aerospace Science and Technology, 2026, 11(1), 20-35
https://www.scirp.org/journal/aast
ISSN Online: 2473-6724
ISSN Print: 2473-6708

Numerical Investigation of Drag Characteristics of a Tiltrotor Wing under Steady Blowing

Xinxin Ouyang, Yun Peng, Guoyi He, Jialin Yu, Wentong Deng

Department of Aeronautics and Astronautics, Nanchang Hangkong University, Nanchang, China
Email: 34016@nchu.edu.cn

How to cite this paper: Ouyang, X.X., Peng, Y., He, G.Y., Yu, J.L. and Deng, W.T. (2026) Numerical Investigation of Drag Characteristics of a Tiltrotor Wing under Steady Blowing. *Advances in Aerospace Science and Technology*, **11**, 20-35.
https://doi.org/10.4236/aast.2026.111002

Received: February 9, 2026
Accepted: March 14, 2026
Published: March 17, 2026

Abstract

During the tilt-transition phase, tiltrotor aircraft experience strong coupling between propeller slipstream and freestream flow. The wing surface flow becomes highly unsteady. Large-scale separation is likely to occur and causes a significant increase in aerodynamic drag. To address this issue, a numerical method for analyzing rotor-wing aerodynamic interference during the tilt-transition phase is developed based on computational fluid dynamics, combined with a momentum-source model. On this basis, a simplified wing-propeller configuration representative of the tilt-transition segment is adopted as the research object, and the aerodynamic characteristics under steady blowing on the lower surface of the wing are systematically investigated. Particular emphasis is placed on the effects of blowing-slot locations at different chordwise positions and of different blowing momentum coefficients on the drag characteristics of the wing. The results show that steady leading-edge blowing effectively weakens the attachment effect of the high-speed propeller slipstream on the lower wing surface. It significantly improves the local pressure distribution and reduces wing drag. As the blowing location moves toward the trailing edge, the coupling between blowing and slipstream tends to induce separation vortices and enlarge the separated region. This leads to a noticeable increase in drag. Proper selection of the blowing location and momentum coefficient can therefore achieve effective drag reduction during the tilt-transition phase.

Keywords

eVTOL, Tiltrotor Aircraft, Momentum Source, Steady Blowing

1. Introduction

In recent years, continuous breakthroughs in aeronautical technology and the

rapid growth of the low-altitude economy have accelerated the development of electric vertical takeoff and landing (eVTOL) aircraft. Owing to their vertical takeoff and landing capability, eVTOL aircraft have attracted significant attention from global investors and research institutions. They are widely regarded as a key technological pathway for the evolution of modern urban air mobility. According to differences in aerodynamic layout and overall configuration, eVTOL aircraft are generally classified into three categories: multi-copter configurations, tilt-thrust (Tilt-X) configurations, and compound wing (Lift + Cruise) configurations [1]. These configurations exhibit substantial differences in aerodynamic characteristics, propulsion systems, and structural design. As a derivative of tiltrotor aircraft, the tiltwing aircraft represents a novel type of vertical takeoff and landing vehicle. It combines features of tiltrotor and multirotor concepts and offers notable advantages in stability, safety, maneuverability, and efficiency. However, due to the unique and variable structural characteristics of tiltwing aircraft, the tilt transition between helicopter mode and fixed-wing mode remains challenging. During this transition, propeller slipstream, freestream flow, and wing-tilting motion are strongly coupled. This coupling results in highly nonlinear aerodynamic behavior and complex physical mechanisms, which significantly increase the difficulty of aerodynamic modeling and analysis.

Globally, the aerodynamic characteristics of tiltrotor aircraft and their derivative configurations during the tilt transition phase have become a major research focus in the aerospace field. Many researchers have conducted in-depth investigations of this complex aerodynamic problem. Droandi [2]-[4] and co-workers performed scaled model experiments to analyze the aerodynamic characteristics during hover and tilt transition. Their results verified the advantage of this configuration in mitigating the download penalty associated with weight increase. The European TILTAERO (Tilt Rotor International Aerodynamics) program also conducted hover tests of tilt-wing configurations. The results showed that the tiltwing layout can effectively alleviate the interference of rotor downwash on the wing in helicopter mode [5] [6]. Zhou Jiasong [7], Chen Pingjian [8], and others investigated the effects of multiple factors on aerodynamic characteristics in hover and forward flight through wind tunnel experiments. Their studies revealed the fundamental variation laws of rotor-wing aerodynamic interference under different operating conditions. Chen Hao and Dong Yuwei [9] [10] carried out systematic analyses of the influence of steady blowing flow control on the download of tiltrotor aircraft. The results indicated that, compared with trailing-edge blowing, leading-edge blowing provides higher control efficiency in reducing download. In addition, the download reduction effect is less sensitive to the blowing momentum coefficient. On this basis, Chen Hao and co-workers further investigated the effects of steady trailing-edge blowing control on the aerodynamic characteristics of the A821201 airfoil for tiltrotor applications. The results showed that, with an appropriate negative blowing angle and a relatively high blowing momentum coefficient, steady trailing-edge blowing can significantly improve the lift characteris-

tics and aerodynamic efficiency of the tiltrotor airfoil.

In the present study, a numerical method based on computational fluid dynamics (CFD) combined with a momentum source model is established to effectively simulate the aerodynamic interference between propeller slipstream and wing during the tilt transition phase. Using this method, the variation law and underlying mechanism of wing drag characteristics under steady blowing on the lower wing surface are systematically analyzed. The results provide a reliable theoretical basis for wing drag control and overall aerodynamic performance optimization of tiltwing aircraft during the tilt transition phase.

2. Numerical Simulation Method and Grid Model

2.1. Flow Control Equations and Momentum Source Method

In numerical simulations of rotor aerodynamics, the commonly used approaches mainly include body-fitted CFD methods and momentum source methods. Body-fitted CFD methods require the generation of body-fitted meshes around each blade. This significantly increases the total number of grid cells and thus reduces computational efficiency [11]. In contrast, the momentum source method replaces the rotor with an actuator disk. The effect of the blades on the flow is represented by momentum source terms. This approach preserves the essential characteristics of the rotor-induced downwash flow. It also enables effective simulation of the interference effects of the rotor downwash on the surrounding flow field, such as the fuselage. Because the momentum source method uses a surface mesh over the entire rotor disk instead of body-fitted meshes around individual blades, it avoids complex blade geometry modeling and boundary-layer mesh generation. This greatly reduces the difficulty of mesh generation and the total grid size. As a result, the computational time is significantly reduced. Therefore, this method is widely applied to studies of aerodynamic interactions between the rotor and the fuselage, as well as between the rotor and the wing. Since this study focuses on the aerodynamic interference characteristics between the rotor and the wing, a CFD method based on the momentum source model is adopted. The governing equations for the numerical simulation are the steady Reynolds-averaged Navier–Stokes (RANS) equations. The three-dimensional incompressible Reynolds-averaged Navier–Stokes equations in an inertial coordinate system are given by:

$$\frac{\partial}{\partial t}\int_{\nu} \boldsymbol{W}\mathrm{d}\nu + \int_{\partial\nu}\left(\boldsymbol{F}_c - \boldsymbol{F}_\nu\right)\mathrm{d}s = \int_{\nu} \boldsymbol{S}\mathrm{d}\nu_\omega \tag{1}$$

In Equation (1), $\boldsymbol{W}$ denotes the conservative variables of the flow field; $\boldsymbol{F}_c$ represents the convective flux; $\boldsymbol{F}_\nu$ denotes the viscous flux; and $\boldsymbol{S}$ is the source term. The symbol ν denotes the volume of the control cell, $\mathrm{d}\nu$ represents the surface of the control cell, and $\mathrm{d}s$ denotes the area of the control cell.

In the momentum source model, the rotor is equivalently simplified as an actuator disk to represent the overall influence of the rotor on the surrounding flow field. Distributed momentum sources are introduced on the actuator disk to sim-

ulate the mechanism by which rotor aerodynamic loads act on the flow field. As shown in Figure 1, the rotor disk is discretized into a number of elemental segments. For an arbitrary disk element, the distance from the disk center is denoted by r. The radial length, corresponding to the width of the blade element, is $\mathrm{d}r$. The associated azimuthal spacing is $\Delta\psi$, and its width is $r\Delta\psi$.

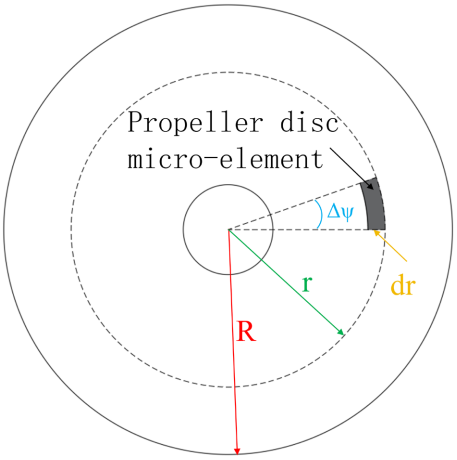

Figure 1. Schematic of the rotor disk plane and the derivation of the momentum source.

The schematic of the aerodynamic forces acting on the blade section and the incoming flow at the blade element is shown in Figure 2. In the blade section coordinate system, the airflow velocities at the blade element are V_O and V_Z. The blade installation angle is φ. Therefore, the effective angle of attack of the blade section is given by:

$$\alpha = \varphi - \beta_* \tag{2}$$

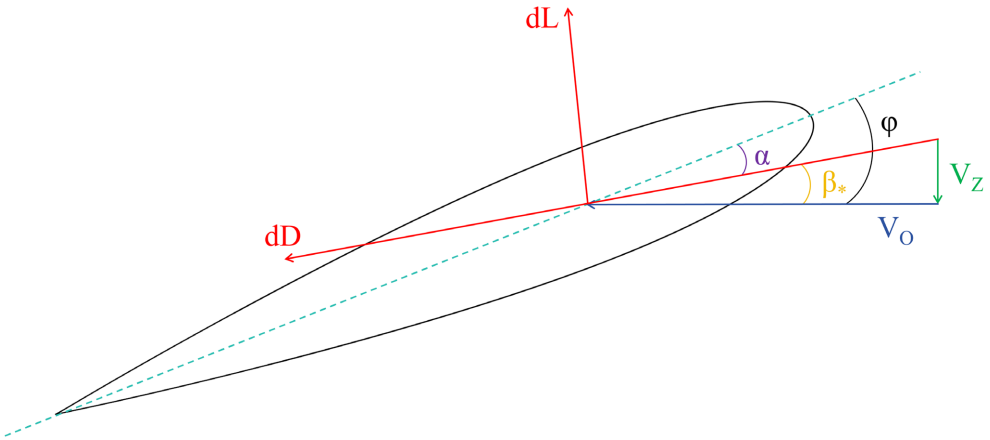

Figure 2. Schematic of blade section aerodynamics and incoming flow.

The aerodynamic characteristics of the airfoil are obtained by querying the airfoil aerodynamic database using the blade section angle of attack and Mach number. Interpolation is then performed to determine the lift and drag coefficients, C_L and C_D. The lift and drag forces of the blade section are given by:

$$\mathrm{d}L = \frac{1}{2}\rho V^2 C_l c \cdot \mathrm{d}r \tag{3}$$

$$\mathrm{d}D = \frac{1}{2}\rho V^2 C_d c \cdot \mathrm{d}r \tag{4}$$

In Equation (3), ρ denotes the air density, and c is the airfoil chord length at the blade element. The lift and drag forces are transformed into the thrust and resistance of the blade section:

$$\mathrm{d}T = \mathrm{d}L\cos\beta_* - \mathrm{d}D\sin\beta_* \tag{5}$$

$$\mathrm{d}Q = -\mathrm{d}L\sin\beta_* - \mathrm{d}D\cos\beta_* \tag{6}$$

Neglecting the radial force acting on the blade element, the force on the blade element in the rotor disk Cartesian coordinate system is denoted as $\mathrm{d}F = \mathrm{d}T + \mathrm{d}Q$. According to Newton's third law, the force exerted by the blade element on the air is $\mathrm{d}F^* = -\mathrm{d}F$, which is an instantaneous force. The time required for one complete rotor revolution is $2\pi/\Omega$, and the time required to rotate through an azimuth angle $\Delta\psi$ is $\Delta\psi/\Omega$. The force exerted by a single blade on the airflow at this element per unit time is $\mathrm{d}F^* \cdot (\Delta\psi/\Omega) \cdot (\Omega/2\pi) = \mathrm{d}F^* \cdot (\Delta\psi/2\pi)$. Over one rotor revolution, the force acting on the airflow at this element per unit time is:

$$S_\Delta^* = N_b \cdot \mathrm{d}F^* \cdot \frac{\Delta\psi}{2\pi} \tag{7}$$

In Equation (7), S_Δ^* denotes the momentum source term, and N_b is the number of rotor blades. The momentum source term is applied over a grid region. This region consists of a collection of individual cells. During the computation, the momentum source term must be applied to each cell within the region. Therefore, the momentum source term acting on a single cell is given by:

$$\mathrm{d}S_\Delta^* = \frac{N_b \cdot \mathrm{d}F^* \cdot \dfrac{\Delta\psi}{2\pi}}{V_{cell}} \tag{8}$$

In Equation (8), V_{cell} denotes the grid cell volume to which the momentum source term is applied.

This paper utilizes the general computational fluid dynamics software STAR-CCM for simulation analysis. An incompressible flow solver is used for the calculations. The convective term is discretized using the Roe scheme, while the viscous term is discretized using the central difference scheme. The turbulence model employed is the K-Omega turbulence model.

2.2. Verification of Momentum Source Method

Based on the data reported in document [12], the momentum source method is validated. The main parameters of the propeller are listed in the following **Table 1**.

In this section, the momentum source method is employed to numerically simulate the hovering motion of a propeller. Local dynamic pressure distributions are monitored at two radial positions of $0.215R$ and $0.325R$ from the propeller disk

center, where R denotes the propeller radius. The numerical results are compared with corresponding experimental measurements, as shown in Figure 3. In the figure, r represents the radial distance from the measurement point to the propeller disk center, and r/R is used to nondimensionalize the radial position. The comparison indicates that the numerical predictions agree well with the experimental data overall. This demonstrates the reliability of the adopted numerical method in predicting the flow-field characteristics of a hovering propeller.

Table 1. Propeller specific parameters table.

Parameter	Data
Blade airfoil	NACA0012
Number of blades	2
blade angle (deg)	11
Blade radius (m)	0.914
The blade chord length (m)	0.1
propeller speed (rad·s^{-1})	122.2
Propeller off-ground height (m)	3.29

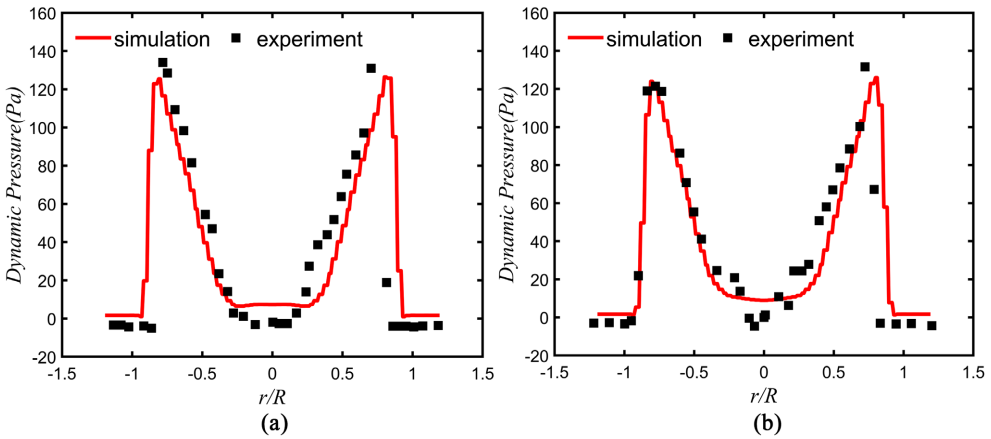

Figure 3. Comparison of the flow-field dynamic pressure distribution beneath the rotor with experimental data. (a) 0.215*R*; (b) 0.325*R*.

2.3. Computational Models and Grid Generation

To investigate the effect of steady blowing on the lower surface of the wing on the drag characteristics of a tilt-wing aircraft during the transition phase, a preliminary geometric model of the tilt-wing aircraft was established, as shown in Figure 4. To avoid the influence of wing geometric parameters, such as sweep angle and dihedral angle, on the aerodynamic analysis, a rectangular straight wing with the simplest structural configuration was adopted. A symmetric airfoil, NACA 0012, was selected to reveal the fundamental interference mechanisms between the propeller slipstream and the freestream under steady blowing conditions. In the proposed model, the wing consists of a fixed wing section and a tilting wing section.

The tilting section can rotate to accommodate different flight modes. The tilt angle is defined as 90˚ in helicopter mode and 0˚ in fixed-wing mode. The half-span of the fixed section is 0.225 m, and that of the tilting section is 0.8 m. The chord length of the wing is 0.12 m. The detailed parameters are listed in Table 2.

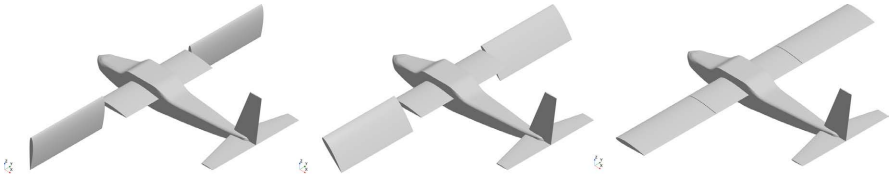

Figure 4. Geometric model of tilt-wing aircraft. (a) Helicopter mode; (b) Tilting transition mode; (c) Fixed wing mode.

Table 2. Calculate the model parameters.

Parameter	Data
wing airfoil	NACA0012
Tilt section wing length (m)	0.8
Wing chord length (m)	0.12
Tilt section wing reference area (m^2)	0.096
Blade radius (m)	0.183
The blade chord length (m)	0.02
number of blade	2
blade angle (deg)	11
Blade airfoil	NACA 0012

The present study focuses on the aerodynamic interference mechanisms between the propeller slipstream and the wing under steady blowing conditions. To effectively reduce the computational cost and highlight the key research objectives, the configuration is reasonably simplified. The aerodynamic interactions involving the fuselage, tail surfaces, and other aircraft components are not considered at this stage. Therefore, the computational model is reduced to a combination of a tiltrotor wing segment and a propeller. Five blowing holes are uniformly arranged with a spacing of 20 mm in the region where the slipstream influence on the lower surface of the wing is most pronounced. The detailed layout is shown in Figure 5. The nondimensional distance of the blowing hole from the wing leading edge is defined as $X_j = x/c$, where c denotes the wing chord length and x is the distance from the leading edge of the blowing hole to the wing leading edge. The nondimensional distance between the propeller center and the wing root is defined as $Y_r = y_r/B$, where y_r is the distance from the propeller center to the root of the tiltrotor wing, and B is the span of the tiltrotor wing segment.

Before performing the CFD simulations, the computational domain of the flow field must be properly defined. The computational domain and boundary condi-

tions are shown in Figure 6. The entire domain is a rectangular region with dimensions of $167c \times 167c \times 67c$, where c denotes the wing chord length. The wing–propeller model is located $42c$ downstream of the velocity inlet. The airflow inlet of the computational domain is specified as a velocity inlet, and the outlet is specified as a pressure outlet. The wing surface is treated as a wall boundary. The blowing holes are modeled using velocity inlet boundary conditions. The blowing momentum coefficient is controlled by prescribing the inlet velocity at the blowing holes. The blowing momentum coefficient C_μ is defined as given in Equation (9). All remaining planar boundaries are set as symmetry planes.

$$C_\mu = \frac{m_j V_j}{\frac{1}{2}\rho_\infty U_\infty^2 S_{ref}} \tag{9}$$

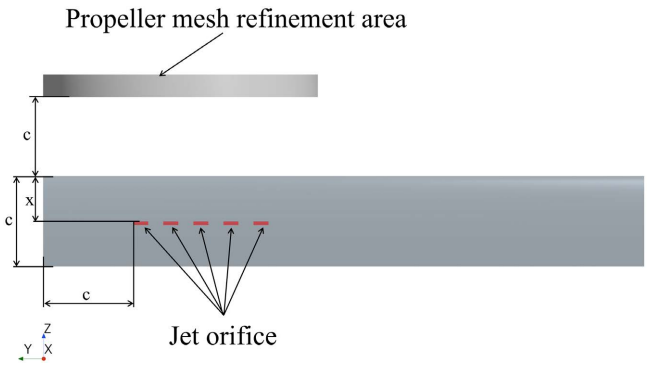

Figure 5. Calculation model.

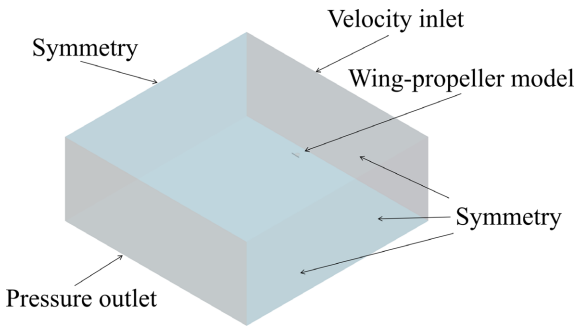

Figure 6. Computational basin and boundary conditions.

The mass flow rate through the blowing outlet per unit time, m_j, is defined as:

$$m_j = \rho_j A_j V_j \tag{10}$$

After obtaining the aerodynamic forces of the wing through simulation, it is necessary to convert them into dimensionless coefficients for comparative analysis under different blowing momentum coefficients. The formulas for calculating the lift coefficient and drag coefficient are as follows:

$$C_L = \frac{L}{\frac{1}{2}\rho U_\infty^2 S_{ref}} \tag{11}$$

$$C_D = \frac{D}{\frac{1}{2}\rho U_\infty^2 S_{ref}} \tag{12}$$

In Equation (9)-(12), V_j denotes the jet velocity; A_j denotes the jet orifice area; ρ_j denotes the air density at the jet exit; ρ_∞ denotes the freestream air density; U_∞ denotes the freestream velocity; and S_{ref} denotes the reference wing area of the tilt-rotor configuration. L is the wing lift. D is the wing drag.

In this study, the computational mesh is generated using an unstructured mesh generation method. The mesh generation process consists of two main stages. First, a high-quality surface mesh and the corresponding computational domain mesh are generated for the numerical model. Subsequently, the interior of the computational domain is filled with volume meshes to form a complete three-dimensional computational mesh system. During surface mesh generation, the upper and lower limits of the mesh size are uniformly specified for the entire computational model. Local mesh refinement is applied in regions with complex wing flow features to ensure numerical accuracy and stability. During volume mesh generation, boundary layer meshes are created on the wing surface to accurately capture the boundary layer flow near the wing. The near-wall grid resolution is controlled to achieve a y^+ value close to 1. The calculation formula is given as follows:

$$y^+ = \frac{u^* y}{\mu} \tag{13}$$

u^* is the friction velocity near the wall. y is the distance between the wall and the first grid node. μ is the kinematic viscosity of the fluid. The calculated height of the first prism-layer cell is 5.31714E−5 m. The number of prism layers is set to 10, and the grid growth rate is 1.2.

In this study, the momentum source method is adopted to represent the propeller for aerodynamic analysis. Therefore, local volumetric mesh refinement is applied to the virtual disk region at the propeller installation location to improve the resolution of the flow field. Specifically, a cylindrical computational domain is defined within the propeller-affected region, with a radius of 0.2 m and a height of 0.03 m. Volumetric mesh refinement is performed within this domain. The final mesh consists of 6.38 million cells. Figure 7 illustrates the mesh of the computational domain and the surface mesh distribution on the wing.

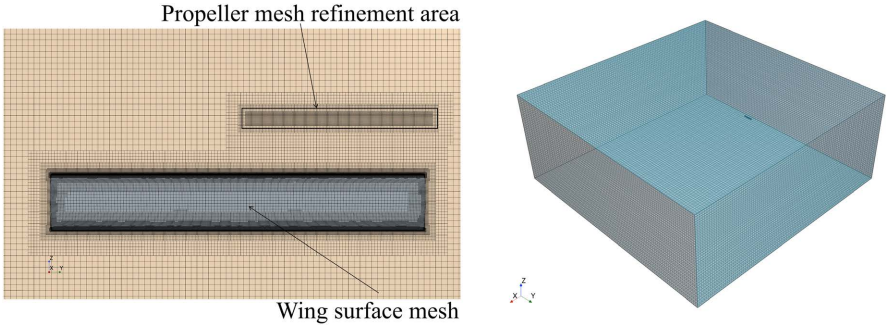

Figure 7. Computing model grid.

2.4. Grid Independence Verification

To verify whether the grid adopted in this study satisfies the computational requirements, a grid independence study was conducted for the computational model. The test conditions were a wing tilt angle of 70˚, an incoming flow velocity of 10 m/s, and a propeller rotational speed of 1500 RPM. The results are summarized in Table 3. As the number of grid elements increases, the computed results gradually converge and become stable. Considering both the accuracy of the numerical results and the computational efficiency, a grid with 6.38 million elements was selected for the simulations presented in this study.

Table 3. Grid independence verification results.

Number of grids (millions)	lift coefficient
286	0.3881
400	0.3807
638	0.3798
786	0.3799

3. Results and Analysis

3.1. The Influence of the Chordwise Position of the Blowhole on the Wing Resistance

3.1.1. Calculation Result

As shown in Figure 8, the drag coefficient curves of the wing vary with different blowing locations. Changes in the chordwise position of the blowing hole significantly modify the surface flow structure and directly affect the drag characteristics of the wing.

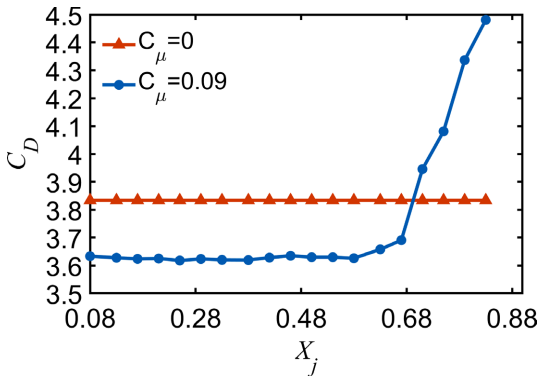

Figure 8. Variation of the drag coefficient with the chordwise position of the blowing hole.

Under the condition of a blowing momentum coefficient of 0.09, placing the blowing holes near the wing leading-edge region results in a pronounced reduction in the overall wing drag compared with the no-blowing baseline. The wing drag coefficient decreases by approximately 5.2%. Further analysis shows that within the near-leading-edge region, as the blowing-hole location moves gradu-

ally downstream along the chord, the wing drag coefficient varies to some extent, but the overall change remains small. However, as the blowing location is moved further toward the trailing edge, that is, to larger values of ($X_j \geq 0.68$), the wing drag coefficient exhibits a clear increasing trend. In particular, when the blowing holes are located near the wing trailing-edge region ($X_j = 0.8$), the blowing fails to effectively suppress adverse flow structures and instead leads to a significant increase in drag. Quantitative results indicate that, under this condition, the wing drag coefficient increases by 14.44% relative to the no-blowing baseline.

3.1.2. Analysis of Effect

Figure 9 presents the velocity contours and pressure coefficient distributions at the spanwise location $Y_r = 0.67$ under steady blowing applied at the wing leading-edge position ($X_j = 0.08$). Compared with the case without flow control (Figure 9), the introduction of steady blowing significantly alters the flow structure near the lower surface of the wing. Because the blowing slots continuously

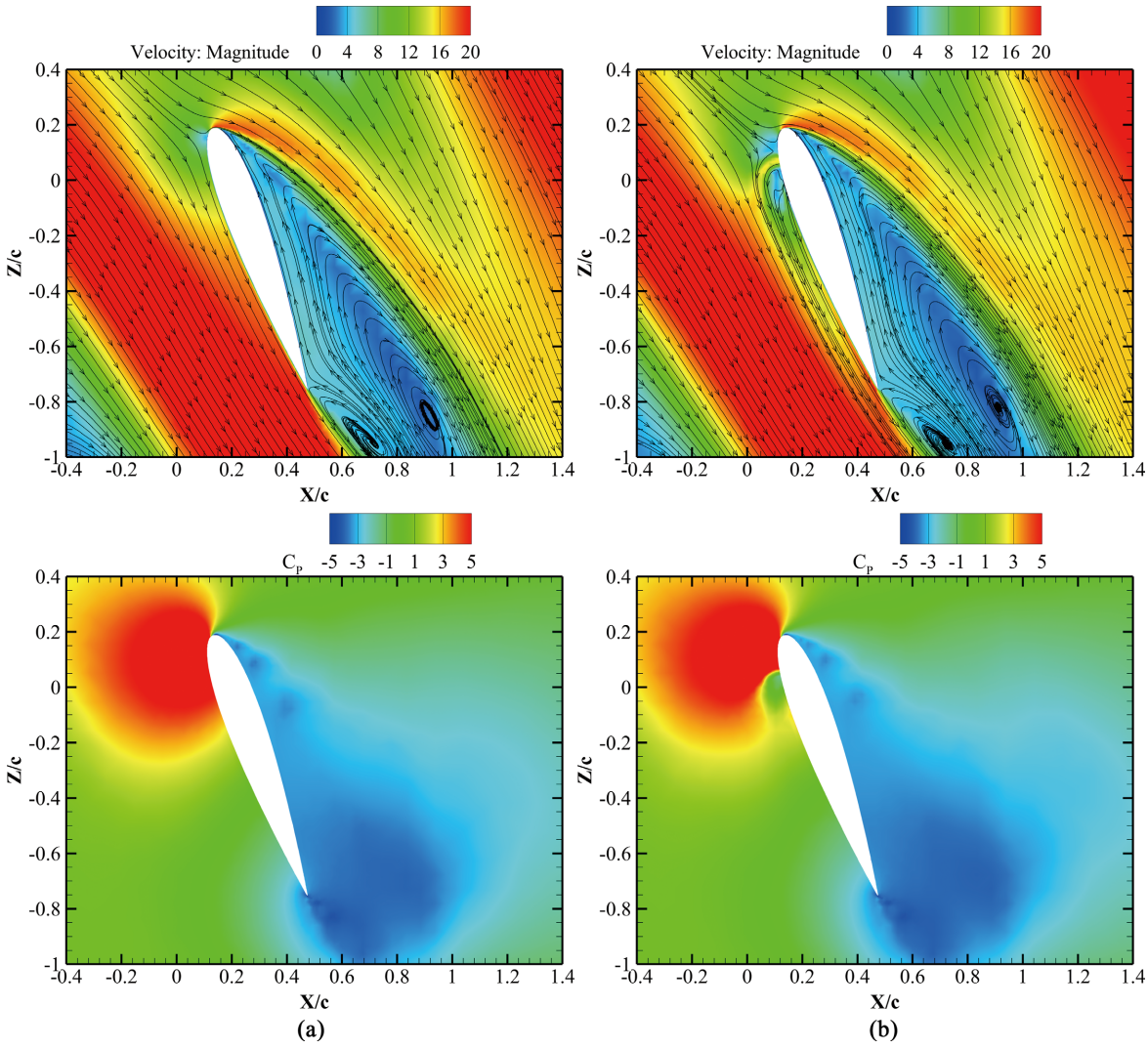

Figure 9. Comparison of velocity cloud map and pressure coefficient cloud map. (a) $C_\mu = 0$; (b) $C_\mu = 0.09$.

inject jets with finite momentum into the external flow, the high-speed slipstream generated by the propeller and originally attached to the lower surface is strongly disturbed. As a result, the region covered by the slipstream is markedly reduced, and the near-wall slipstream velocity over the lower surface decreases substantially.

Based on the pressure coefficient distribution results, further analysis reveals that under the influence of steady blowing, the high dynamic pressure region originally formed by the direct impact of high-speed slipstream on the wing leading edge is significantly weakened. Meanwhile, a distinct region with a lower pressure coefficient appears near the blowing holes. Leading-edge blowing alters the local flow characteristics, thereby reducing the local intensification effect of the high-speed slipstream on the wing leading edge to some extent. In contrast, on the upper surface of the wing, due to the large angle of attack, the flow characteristics are primarily influenced by the incoming flow. Regardless of whether steady blowing control is applied, the flow remains in a large-scale separation state, with little variation in the overall flow field structure and pressure coefficient distribution.

A comparative analysis of the flow-field structures with the blowing slot located at different chordwise positions was conducted to investigate the influence of blowing location on the aerodynamic drag characteristics of the wing. **Figure 10** presents the velocity contours and pressure coefficient distributions at a spanwise wing section for a blowing momentum coefficient of $C_\mu = 0.09$. The chordwise

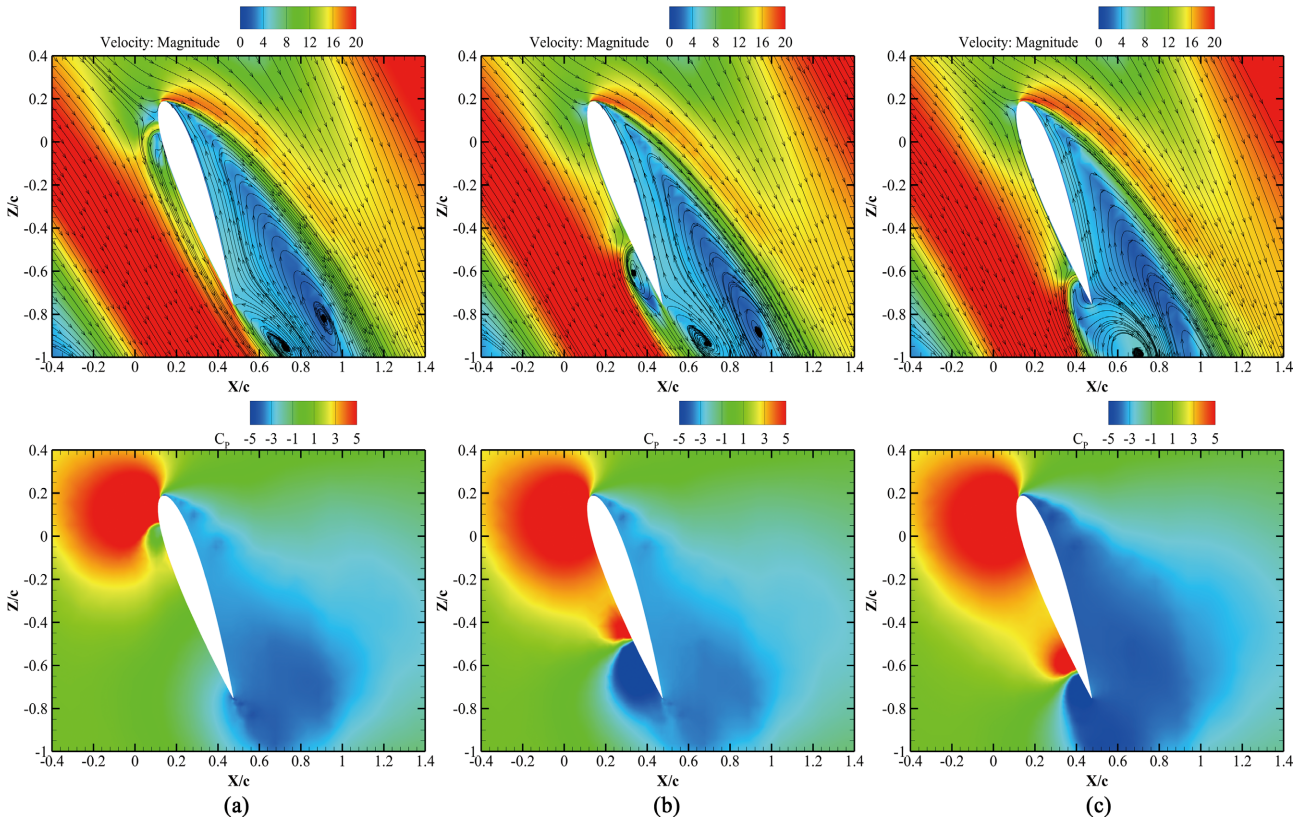

Figure 10. Velocity contour plot of the cross-sectional plane at $C_\mu = 0.09$, $Y_r = 0.67$. (a) $X_j = 0.08$; (b) $X_j = 0.68$; (c) $X_j = 0.83$.

locations of the blowing slot are $X_j = 0.08$, $X_j = 0.68$, and $X_j = 0.83$.

From the flow-field structures shown in the figure, as the blowing-slot location moves downstream along the wing chord toward the trailing edge, the attached region of the high-speed slipstream on the lower surface exhibits a clear reduction. When the blowing slot is located near the trailing edge ($X_j = 0.68$), the jet issued from the slot interacts with the high-speed propeller slipstream, which significantly alters the local flow structure and generates small-scale separation vortices. The appearance of these vortices disrupts the originally attached flow on the lower surface and subsequently induces a pronounced low-pressure region locally on the lower wing surface. When the blowing slot is placed at the trailing-edge position ($X_j = 0.83$), the separation vortex induced by the jet on the lower surface convects around the trailing edge and couples with the separation vortex on the upper surface, leading to a further expansion of the separated region.

Based on the pressure coefficient contours, the blowing has a pronounced effect on the surface pressure distribution of the wing. As the blowing location moves progressively toward the trailing edge, the region of high dynamic pressure near the leading edge exhibits a clear expansion. Meanwhile, the low-pressure region on the upper surface of the wing increases significantly in extent, and the pressure coefficient within this region decreases further. This change results in a larger surface pressure gradient, which in turn leads to a substantial increase in wing drag.

3.2. Effect of Blowing Momentum Coefficient on Wing Drag

3.2.1. Calculation Result

With the blowing slot located at $X_j = 0.08$, the influence of the blowing momentum coefficient on the drag characteristics of the wing is further investigated. Numerical simulations are conducted for blowing momentum coefficients of 0, 0.042, 0.06, and 0.09. The effects of different jet intensities on the wing drag characteristics are analyzed and compared.

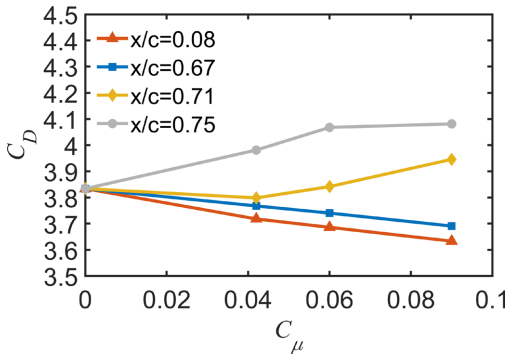

Figure 11. Variation curve of drag coefficient with blowing momentum coefficient.

From the variation of the drag coefficient of the tilt-wing during the transition phase under different blowing momentum coefficients (see **Figure 11**), it is evident that the blowing location has a significant influence on the drag characteristics. When the blowing slot is located near the leading edge of the transition wing

($X_j = 0.08$), the blowing control exhibits a pronounced drag-reduction effect. As the blowing momentum coefficient increases, the drag coefficient decreases steadily and monotonically. The minimum drag coefficient occurs at $C_\mu = 0.09$. Compared with the no-blowing condition $C_\mu = 0$, the drag coefficient is reduced by approximately 5.2%. When the blowing location is placed in the mid-to-rear region of the wing, the drag coefficient still decreases with increasing blowing momentum coefficient. However, the magnitude of the reduction is clearly smaller than that of the leading-edge blowing case. This result indicates that the effectiveness of flow control and drag reduction is weakened at these locations. In contrast, as the blowing location moves further downstream, the drag-reduction effect gradually diminishes and may even reverse. At $X_j = 0.71$, the drag coefficient exhibits a non-monotonic trend with respect to the blowing momentum coefficient. It first decreases and then increases. The optimal drag-reduction effect at this position occurs at $C_\mu = 0.042$. When the blowing slot is located at the trailing edge, blowing fails to reduce drag. Instead, the drag coefficient increases significantly as the blowing momentum coefficient increases.

3.2.2. Analysis of Effect

Figure 12 presents the flow-field characteristics at a blowing location of $X_j = 0.08$ under different blowing momentum coefficients. As shown in the figure, without blowing ($C_\mu = 0$), the high-speed slipstream generated by the propeller remains closely attached to the lower surface of the wing. Meanwhile, the wing leading edge is directly impinged by the high-speed slipstream, forming a region of high dynamic pressure. As the blowing momentum coefficient increases, the blowing jet introduces a pronounced disturbance to the original slipstream structure. Consequently, the intensity of the high-speed slipstream attached to the wing

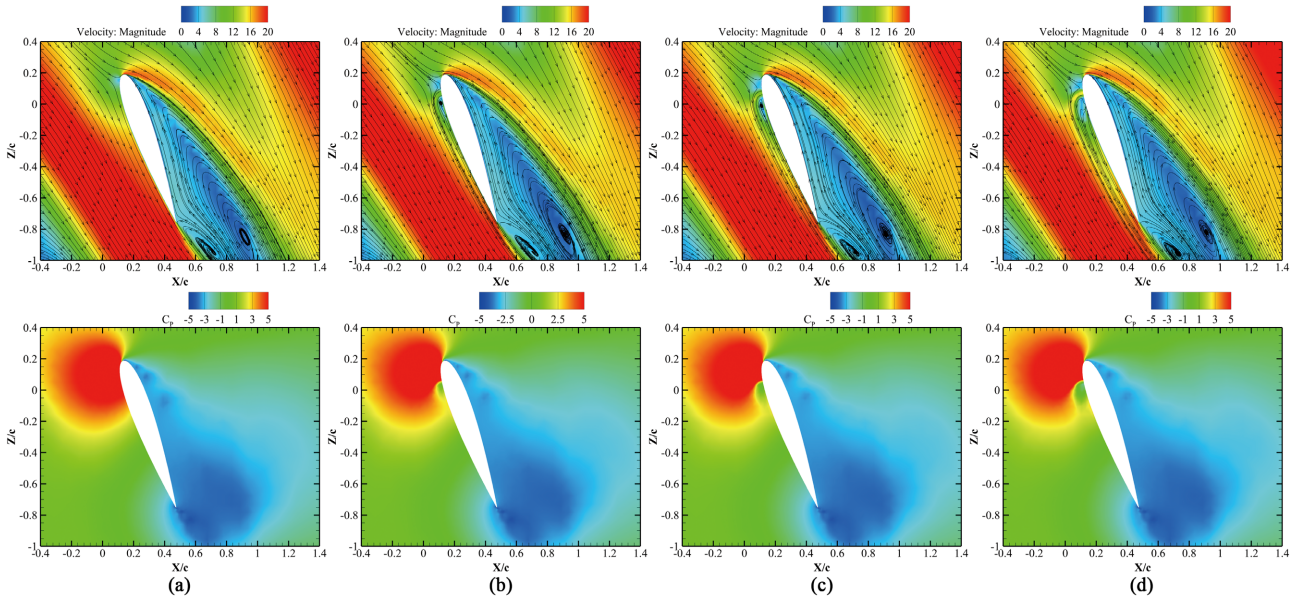

Figure 12. Velocity contour plot on the cross section at $X_j = 0.08$, $Y_r = 0.67$. (a) $C_\mu = 0$; (b) $C_\mu = 0.042$; (c) $C_\mu = 0.06$; (d) $C_\mu = 0.09$.

lower surface gradually weakens, and its velocity exhibits a continuous decreasing trend. Further examination of the pressure coefficient contours indicates that, with increasing blowing momentum coefficient, the extent of the high dynamic pressure region around the blowing orifices shrinks markedly. In addition, the local pressure concentration near the wing leading edge is effectively alleviated.

4. Conclusions

This paper investigates the aerodynamic characteristics of a tiltwing aircraft during the tilt-transition phase. The study focuses on the effects of steady blowing applied to the lower surface of the wing on its drag characteristics. By comparing the computational results, the following conclusions are obtained.

1) The chordwise location of the blowing slots has a significant influence on the surface flow structure and drag characteristics of the wing. At a blowing momentum coefficient of 0.09, when the blowing slots are located near the leading edge, steady blowing effectively interferes with the attachment of the high-speed propeller slipstream to the lower wing surface. This interaction weakens the local concentration of high dynamic pressure near the leading edge. As a result, a pronounced drag reduction is achieved, and the wing drag coefficient is reduced by approximately 5.2% compared with the baseline case without blowing.

2) Within the region near the leading edge, small chordwise displacements of the blowing slots have a relatively limited effect on the drag coefficient. However, as the blowing location moves further toward the trailing edge, the lower-surface flow structure deteriorates. Local separation vortices gradually form and develop, leading to a significant increase in wing drag. In particular, when the blowing slots are located near the trailing edge, the drag coefficient increases by 14.44% relative to the no-blowing condition.

3) When the blowing slots are located near the leading edge, the wing drag coefficient during the tilt-transition phase exhibits a stable and monotonic decrease with increasing blowing momentum coefficient, resulting in the most pronounced drag-reduction effect. When the blowing location is in the mid-to-aft region of the wing, the drag coefficient still decreases as the blowing momentum coefficient increases, but the magnitude of drag reduction is significantly reduced. In contrast, when the blowing slots are placed close to the trailing edge, the drag coefficient shows a non-monotonic dependence on the blowing momentum coefficient, and steady blowing not only fails to reduce drag but instead increases the wing drag.

Funding

This work was supported by National Natural Science Foundation of China (12362026), Nanchang University of Aeronautics and Astronautics Graduate Student Innovation Special Funds Programme (Provincial-Level Project: YC2024-S624).

Conflicts of Interest

The authors declare no conflicts of interest regarding the publication of this paper.

References

[1] Li, G.S. (2025) Review of Typical eVTOL Aircraft Configuration and Propulsion System Design Methods. *Journal of Guilin Institute of Aerospace Industry*, **30**, 707-722.

[2] Droandi, G., Gibertini, G., Grassi, D., Campanardi, G. and Liprino, C. (2016) Proprotor-Wing Aerodynamic Interaction in the First Stages of Conversion from Helicopter to Aeroplane Mode. *Aerospace Science and Technology*, **58**, 116-133. https://doi.org/10.1016/j.ast.2016.08.013

[3] Droandi, G., Zanotti, A. and Gibertini, G. (2015) Aerodynamic Interaction between Rotor and Tilting Wing in Hovering Flight Condition. *Journal of the American Helicopter Society*, **60**, 1-20. https://doi.org/10.4050/jahs.60.042011

[4] Droandi, G., Zanotti, A., Gibertini, G., Grassi, D. and Campanardi, G. (2015) Experimental Investigation of the Rotor-Wing Aerodynamic Interaction in a Tiltwing Aircraft in Hover. *The Aeronautical Journal*, **119**, 591-612. https://doi.org/10.1017/s0001924000010708

[5] Visingardi, A., Khier, W. and Decours, J.J.D. (2004) The Blind Test Activity of TILTAERO Project for the Numerical Aerodynamic Investigation of a Tiltrotor. *European Congress on Computational Methods in Applied Sciences and Engineering*, *ECCOMAS* 2004, Jyväskylä, 24-28 July 2004, 1-20.

[6] Jimenez Garcia, A. and Barakos, G.N. (2017) Numerical Simulations on the ERICA Tiltrotor. *Aerospace Science and Technology*, **64**, 171-191. https://doi.org/10.1016/j.ast.2017.01.023

[7] Zhou, J.S. (2004) Research on Rotor/Wing Interference of Tilt-Rotor Aircraft in Hover. Master's Thesis, Nanjing University of Aeronautics.

[8] Chen, P.J., Lin, Y.F. and Huang, S.L. (2008) Experimental Study on Rotor/Wing Aerodynamic Interference of Tiltrotor Aircraft. *Helicopter Technology*, **9**, 107-115.

[9] Chen, H. and Dong, Y.W. (2021) The Effect of Steady Blowing on the Downward Load of Tilt-Rotor Aircraft. *Journal of Applied Mechanics*, **38**, 93-98.

[10] Chen, H., Hu, H.Y. and Yang, D.C. (2024) Effect of Trailing Edge Steady Blowing on Aerodynamic Performance of Tiltrotor Airfoil. *Computer Simulation*, **41**, 23-28.

[11] Huang, Q., He, G., Jia, J., Hong, Z. and Yu, F. (2024) Numerical Simulation on Aerodynamic Characteristics of Transition Section of Tilt-Wing Aircraft. *Aerospace*, **11**, Article 283. https://doi.org/10.3390/aerospace11040283

[12] Li, P., Zhao, Q. and Zhu, Q. (2015) CFD Calculations on the Unsteady Aerodynamic Characteristics of a Tilt-Rotor in a Conversion Mode. *Chinese Journal of Aeronautics*, **28**, 1593-1605. https://doi.org/10.1016/j.cja.2015.10.009